Int. J. Electrochem. Sci., 12 **(2017)** 11778 – 11788, doi: 10.20964/2017.12.41

International Journal of
ELECTROCHEMICAL
SCIENCE
www.electrochemsci.org

Elliptical Fe_2O_3 Particles / Reduced Graphene Oxide Composite Materials for Supercapacitors and Their Electrochemical Properties in Different Electrolytes

Meirong Li[1,2], *Yurong Ren*[1,2,*], *Haiyan Chen*[3], *Xiaobing Huang*[4], *Jianning Ding*[1,2,5,*]

[1] School of Materials Science and Engineering, Changzhou University, Changzhou 213000, China
[2] Jiangsu Province Cultivation base for State Key Laboratory of Photovoltaic Science and Technology, Changzhou University, Changzhou, 213164
[3] NO. 47. Qingyang North Rd., Tianning district, Changzhou, Jiangsu Province, P. R. China
[4] College of Chemistry and Chemical Engineering, Hunan University of Arts and Science, Changde, 41500, China
[5] Micro/Nano Science and Technology Center, Jiangsu University, Zhenjiang, 212013, China
[*]E-mail: ryrchem@163.com, ryrchem@cczu.edu.cn

Received: 23 July 2017 / *Accepted:* 25 September 2017 / *Published:* 12 November 2017

In this work, a supercapacitor electrode material, Fe_2O_3/rGO composite, was fabricated by the hydrothermal method. A mixture of isopropyl alcohol and deionized water was used as the hydrothermal agent. Structural characterization revealed that the Fe_2O_3 particles in the composites exhibit a unique elliptical structure with significantly increased specific surface area compared to hexagonal Fe_2O_3 particles, thereby allowing more ions to penetrate. The Fe_2O_3/rGO composite has a lager specific capacitance than bare Fe_2O_3 particles in 1M KOH. Additionally, compared to that in 1M Na_2SO_3, 1M Na_2SO_4, 1M KOH and 6M KOH electrolytes, Fe_2O_3/rGO exhibits better electrochemical performance in 6M KOH with 3M methanol.

Keywords: Fe_20_3; rGO composite; hydrothermal method; supercapacitor.

1. INTRODUCTION

The search for new energy storage devices has become a hot topic in the field of new energy. New types of energy devices must be low-cost and environmentally friendly [1,2]. Supercapacitors, also called electrochemical capacitors, display the notable characteristics of high power density, low maintenance cost, fast charging/discharging rate and long cycle life [3-5]. According to their energy storage mechanisms, supercapacitors can be divided into electrical double layer capacitors (EDLCs) and pseudocapacitors. The charge storage capacity of EDLCs depends on the electrostatic force acting

on the interface between the active electrode material and the electrolyte. In contrast, pseudocapacitors utilize fast oxidation/reduction reactions and reversible chemical adsorption/desorption to produce a higher specific capacitance than EDLCs [6,7].

It is well known that the performance of supercapacitors is closely related to the electrode materials [8,9]. Supercapacitor electrode materials are divided into three categories, i.e., carbon materials, conducting polymers and transition metal oxides [10-12]. In particular, transition metal oxides are attractive supercapacitor electrode materials because they have many oxidation states. For example, NiO [13], MnO_2 [14], Co_3O_4 [15], Fe_2O_3 [16], ZnO [17], and TiO_2 [18] transition metal oxide materials have larger specific capacitance and energy density as significant electrode materials for pseudocapacitors than electrical double layer capacitors. Fe_2O_3 is widely used in supercapacitors because of its multivariate oxidation states, environmental compatibility and low cost. However, Fe_2O_3 also exhibits several issues, such as bad rate capability and poor cycling stability as a result of its small specific surface area and poor conductivity [19-21]. Some efforts have been made to overcome these difficulties. For example, carbon-based materials can be composited with Fe_2O_3 as the composite electrode to improve the electrochemical properties and cycling stability of supercapacitors in comparison with pure Fe_2O_3 [22,23].

In this work, we attempted to fabricate Fe_2O_3/rGO composites by a one-step hydrothermal process accompanied using isopropyl alcohol and deionized water as the hydrothermal agent. This method achieved elliptical Fe_2O_3 particles homogeneously covering the surface of the rGO sheets. Such unique architectures can offer many channels for rapid diffusion of electrolyte ions within the active electrode material.

2. EXPERIMENTAL

2.1. Synthesis of the composite

All reagents were purchased from Sinopharm Chemical Reagent. The preparation method of graphite oxide (GO) was the modified Hummers method as described in previous reports [24]. Fe_2O_3/rGO was synthesized as follows: 120 mg of GO was dispersed ultrasonically in a 60-mL mixture (30 mL isopropyl and 30 mL deionized water) for 1 h to form a homogeneous GO solution. Then, 2 g of $FeCl_3$ and 2 g of CH_3COONa were added to the GO solution under magnetic stirring for 30 min. Then, the obtained mixed suspension was transferred to a Teflon-lined autoclave, followed by hydrothermal treatment at 180 °C for 700 min. The sample was collected by naturally cooling to room temperature, then filtered, cleaned with deionized water several times, and finally dried at 60 °C in a vacuum oven for 6 h. For comparison, pure Fe_2O_3 without GO was also fabricated by the above process.

2.2. Structure characterization and electrochemical evaluation

The morphologies of all prepared samples were analysed by scanning electron microscopy (SEM). X-ray diffraction (XRD) measurements were obtained using a D8 (Bruker) X-ray

diffractometer with Cu Kα radiation (λ=1.5418 Å). The mass of rGO in the composite was determined by thermogravimetric analysis (TGA) from room temperature to 1000 °C at a heating rate of 10 °C min^{-1} in air. Raman spectra were obtained using a RM2000 Raman Spectrometer (Renishaw, British).

The working electrode was obtained by mixing 80 wt% active material (Fe_2O_3/rGO or Fe_2O_3), 10 wt% Super P, and 10 wt% sodium alginate. Then, the three components formed a slurry, which was mixed and ground with deionized water. Finally, the slurry was coated onto a nickel foam (1×1 cm^2). The mass of the active electrode material (Fe_2O_3/rGO or Fe_2O_3) was equal to the mass of the foam nickel coated with the active material less the mass of the pure foam nickel. The surface area of the active material (Fe_2O_3/rGO or Fe_2O_3) in the working electrode was 1 cm^2, and the mass of the active material (Fe_2O_3/rGO or Fe_2O_3) was approximately 3 mg.

The three-electrode cell system contained a working electrode, a platinum sheet counter electrode, and a saturated calomel electrode as the reference electrode. Cyclic voltammetry (CV) and galvanostatic charge-discharge (GCD) tests were conducted on an electrochemical workstation, CHI760E, in 1M Na_2SO_3, 1M Na_2SO_4, 1M KOH, and 6M KOH with and without 3M methanol electrolytes. Electrochemical impendence spectroscopy (EIS) tests were performed between 10^5 Hz and 0.01 Hz using an AC amplitude of mV at open circuit potential.

3. RESULTS AND DISCUSSION

3.1. Material characterization

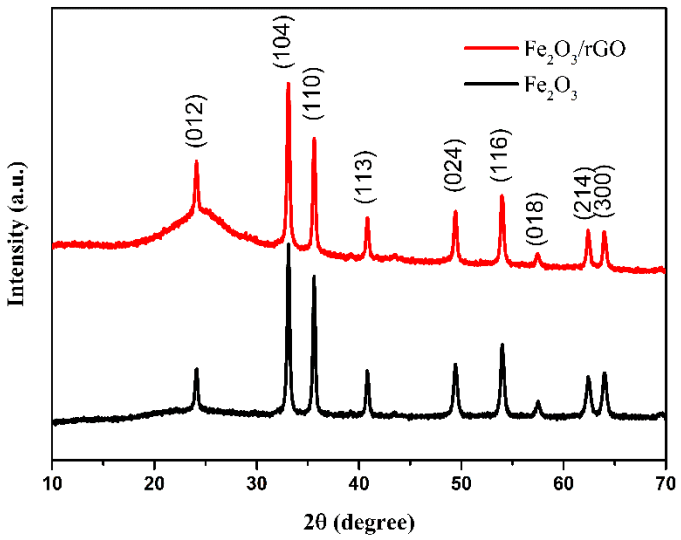

Figure 1. XRD patterns of Fe_2O_3 and Fe_2O_3/rGO

The crystalline structures of the prepared samples (Fe_2O_3/rGO and Fe_2O_3) were identified by XRD. The XRD patterns of Fe_2O_3 and Fe_2O_3/GO are shown in Fig. 1. The diffraction peaks present at 24.1°, 33.2°, 35.6°, 40.9°, 49.5°, 54.1°, 57.6°, 62.4° and 64° represent the (012), (104), (110), (113), (024), (116), (018), (214) and (300) crystal planes, respectively. All of the peaks can be assigned to Fe_2O_3 (JCPDS no. 33-0664), which proves that the Fe_2O_3 was successfully prepared. As described in the literature [25], no significant change in XRD patterns of Fe_2O_3 particles and Fe_2O_3/rGO composite

is observed, which demonstrates that the phase purity of Fe_2O_3 is maintained after formation of the composite. However, in the XRD spectrum, there is no definitive evidence to confirm the presence of GO in the composite.

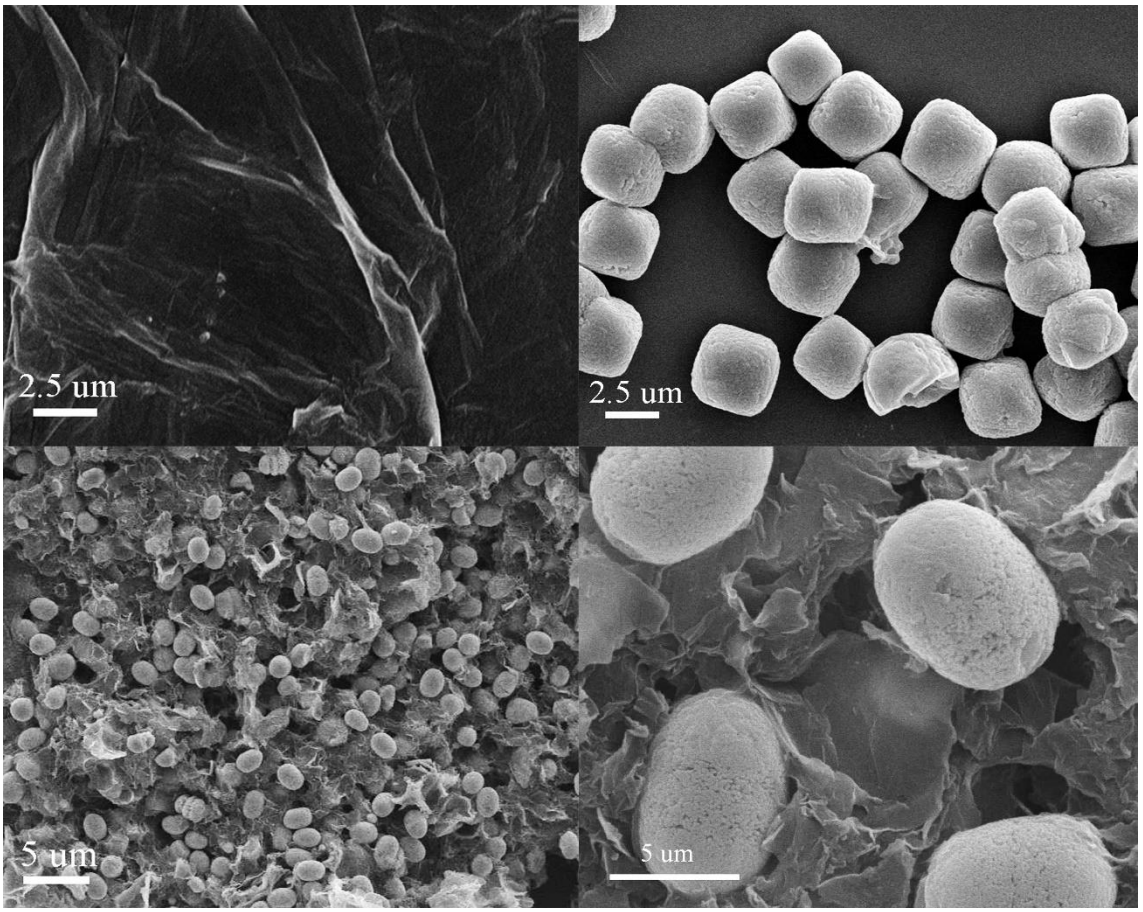

Figure 2. SEM images of rGO (a). Fe_2O_3 (b) and Fe_2O_3/rGO (c,d) at different magnifications

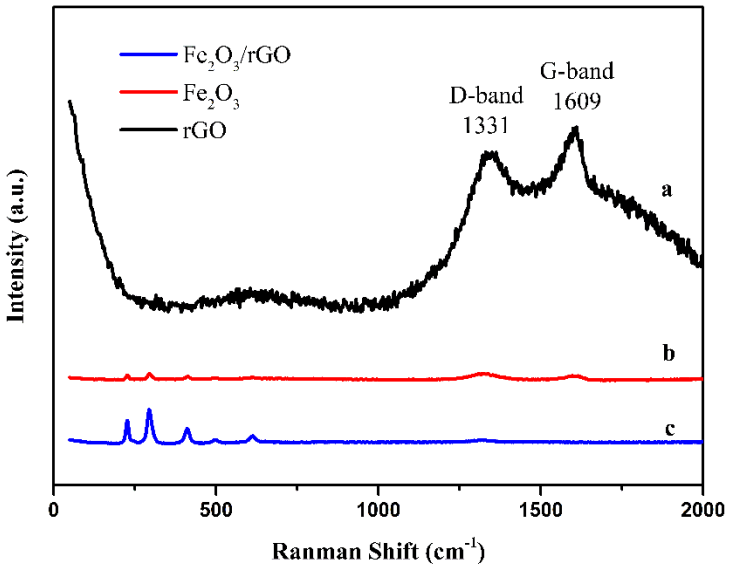

Figure 3. The Raman spectra of rGO (a), Fe_2O_3/rGO (b) and Fe_2O_3 (c)

The morphologies of the prepared samples (rGO, Fe_2O_3/rGO and Fe_2O_3) were studied by SEM. As seen in Fig. 2a, the rGO has a wrinkled porous structure with a framework network. Fe_2O_3 with a uniform grain size of approximately 2.5 um is shown in Fig. 2b. Fig. 2c and Fig. 2d show the SEM images of Fe_2O_3/rGO at different magnifications. In Fig. 2c, the Fe_2O_3 particles are elliptical, which greatly increases the specific surface area compared to hexagonal Fe_2O_3. Additionally, the Fe_2O_3 particles are shown to be evenly distributed on the layer of rGO sheets. As reported in previous work [26], such composite frameworks could enhance the interface contact and suppress the dissolution and agglomeration of particles, thereby promoting the electrochemical activity and stability of the Fe_2O_3/rGO. As shown in the high magnification SEM image (Fig. 2d), the Fe_2O_3 particles exhibit a porous structure.

The Raman spectra of the prepared samples (rGO, Fe_2O_3/rGO and Fe_2O_3) are shown in Fig. 3. The Raman spectrum of rGO is shown in Fig. 3a. The Raman peak of rGO at 1331 cm^{-1} is called the D peak, and its peak intensity is expressed as I_D. The D peak is the defect peak caused by disorder or sp^3 carbon atoms. The Raman peak at 1609 cm^{-1} is called the G peak, and its peak intensity is expressed as I_G. The G peak is a characteristic peak of sp^2 carbon structures. As reported in previous works [27,28], the ratio of I_D to I_G represents the reduction degree of graphene oxide. The I_D/I_G ratio of rGO is 0.81, and the I_D/I_G ratio of Fe_2O_3/rGO is 1.16. The larger I_D/I_G value of Fe_2O_3/rGO suggests that the combination of Fe_2O_3 particles within rGO sheets can improve the structural disorder and defects.

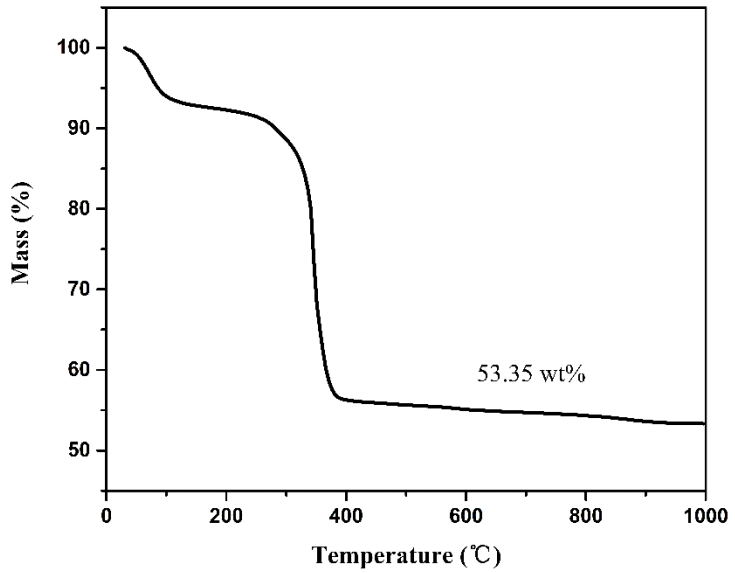

Figure 4. The TGA curve of Fe_2O_3/rGO.

Fig. 4 shows the TGA curve of Fe_2O_3/rGO, which was heated to 1000 °C in air. We observed that the first mass loss between 35~100 °C may be attributed to the decomposition of individual precursors. As the temperature rises, a second rapid mass loss occurs between 250~400 °C corresponding to the oxidation of carbon. According to the mass change, the mass ratio of Fe_2O_3 particles in the composites was calculated to be 55%.

3.2. Electrochemical properties

Fig. 5a shows the CV curves of the prepared electrode (Fe_2O_3 and Fe_2O_3/rGO) in 1 M KOH electrolytes at a scan rate of 10 mV s^{-1}. The curve shape of Fe_2O_3 was irregular, and the redox peaks were obscure, corresponding to conversion between Fe^{2+} and Fe^{3+} [29,30]. However, the Fe_2O_3/rGO composite electrode showed obvious strong oxidation and reduction peaks. The specific capacitance of the active electrode material is well known to be proportional to the area of the CV curve, which suggests that the Fe_2O_3/rGO composite has a higher capacitance than bare Fe_2O_3. As shown in Fig. 5b, a charge platform at approximately -0.7 V and a discharge platform at approximately -1.0 V correspond to the oxidation and reduction of Fe_2O_3 particles, respectively.

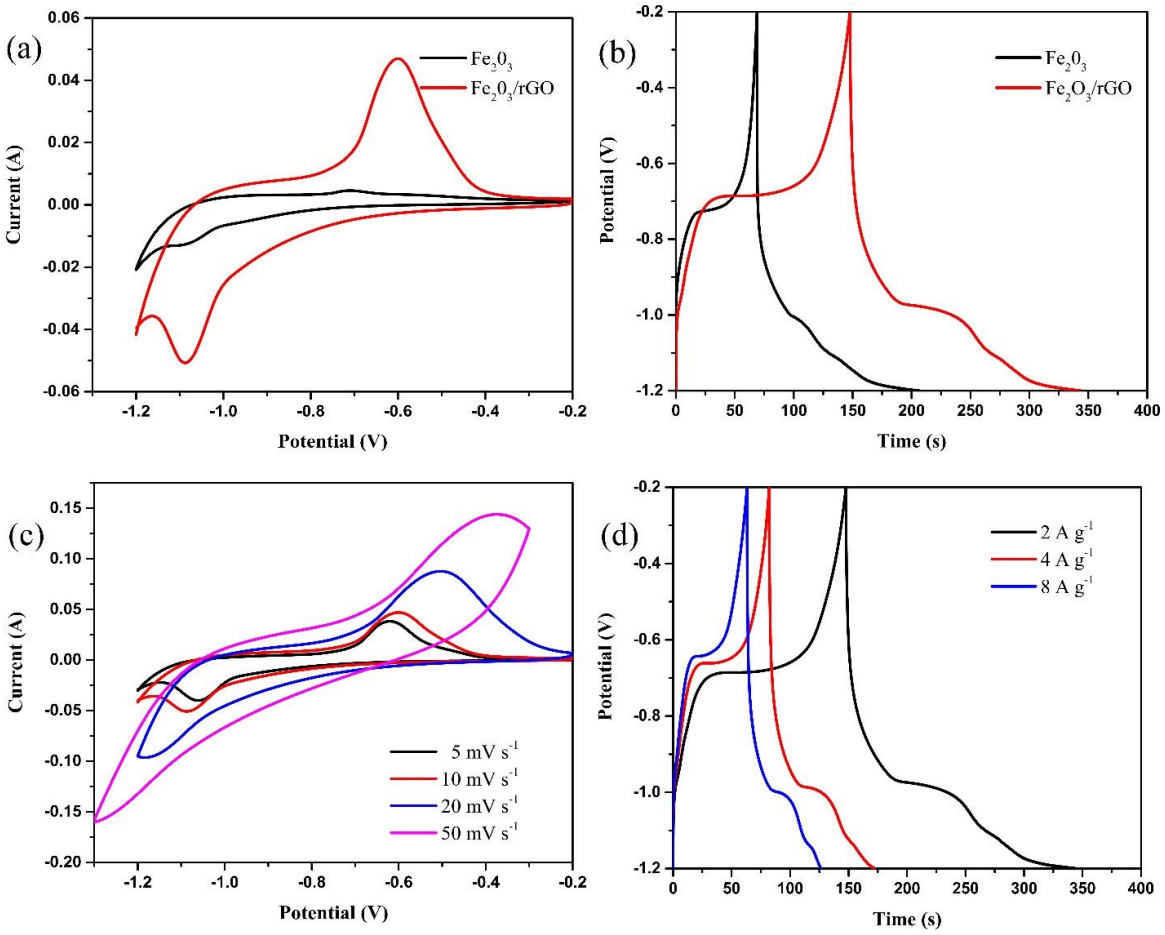

Figure 5. (a) CV curves of Fe_2O_3 and Fe_2O_3/rGO electrodes in 1M KOH electrolytes at scan rate of 10 mV s^{-1}. (b) GCD curves of Fe_2O_3 and Fe_2O_3/rGO electrodes in 1M KOH electrolytes at a current density of 2 A g^{-1}. (c) CV curves of Fe_2O_3/rGO electrode in 1M KOH electrolytes at different scan rates. (d) GCD curves of Fe_2O_3/rGO electrode in 1M KOH electrolytes at different current densities.

The mass-specific capacitance of bare Fe_2O_3 particles (260 F g^{-1}) was calculated to be smaller than that of Fe_2O_3/rGO (400 F g^{-1}). As reported in previous works [31,32], Fe_2O_3/rGO has better electrochemical performance because of the contribution of the pseudocapacitance of Fe_2O_3 and the

EDL capacitance of rGO in the composite. From Fig. 5c, the Fe_2O_3/rGO composite exhibits an oxidation peak and a reduction peak at 0.621 V and -1.061 V, respectively, at a scan rate of 5 mV s^{-1}, corresponding to the redox process. The oxidation peak of the Fe_2O_3/rGO composite was found at -0.504 V at a scan rate of 20 mV s^{-1}. However, the reduction peak was obscure. At a higher scan rate of 50 mV s^{-1}, the oxidation peak was broadened, which may occur when the transfer between the ion of the active material and the ion of the electrolyte is not consistent with the electron transfer of the external circuit. As a result, the accumulated electrons on the electrode would increase potential for charging and decrease potential for discharging. The GCD curves of Fe_2O_3/rGO are shown in Fig. 5d. The charge/discharge curves show the Faraday characteristics of the Fe_2O_3/rGO electrode.

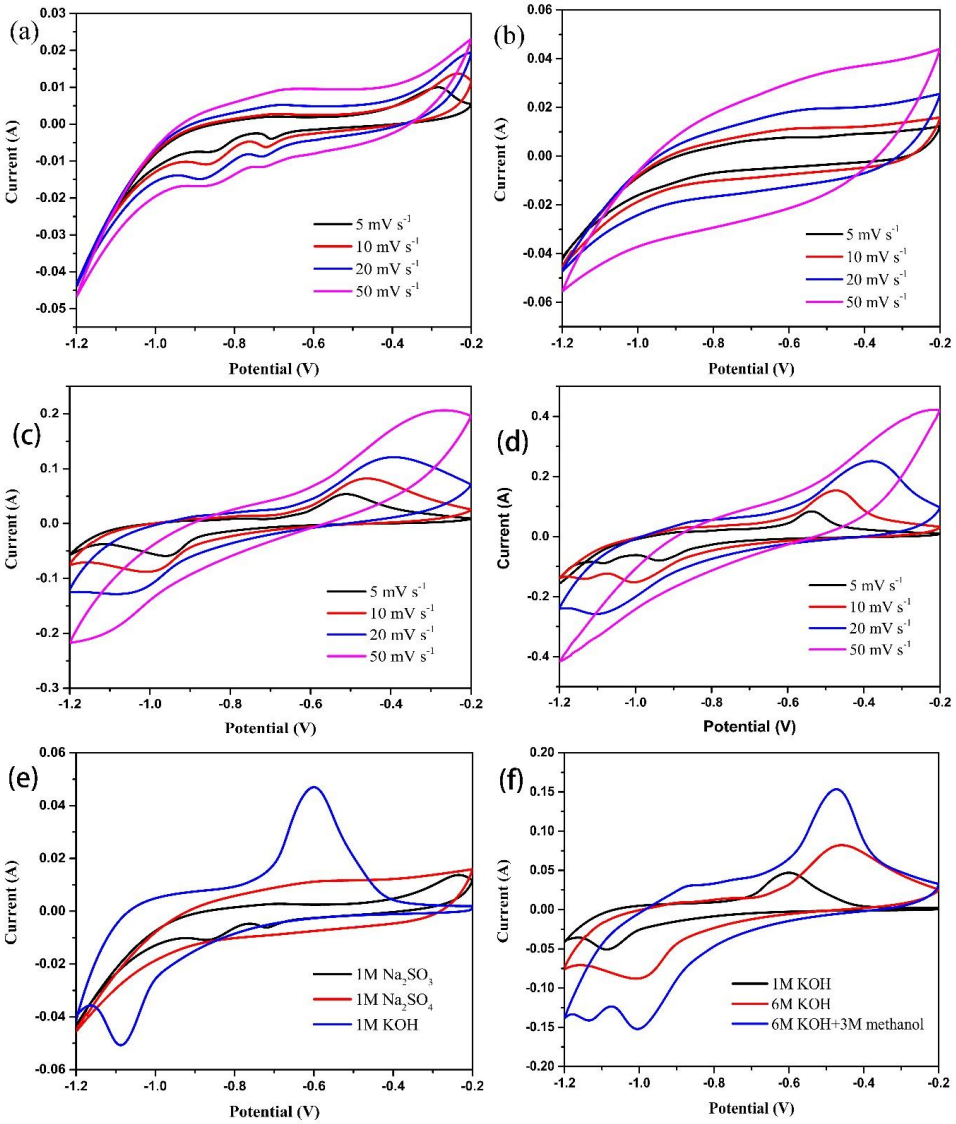

Figure 6. CV curves of Fe_2O_3/rGO electrode (a) in 1M Na_2SO_3 electrolytes at different scan rates. (b) in 1M Na_2SO_4 electrolytes at different scan rates. (c) in 6M KOH electrolytes at different scan rates. (d) in 6M KOH with 3M methanol electrolytes at different scan rates. (e) in 1M Na_2SO_3, 1M Na_2SO_4 and 1M KOH electrolytes at a scan rate of 10 mV s^{-1} respectively. (f) in 1M KOH, 6M KOH with and without 3M methanol electrolytes at the scan rate of 10 mV s^{-1} respectively.

Fig. 6a shows the CV curves of the Fe_2O_3/rGO electrode in 1 M Na_2SO_3 at different scan rates. There is an oxidation peak at -0.283 V and a reduction peak at -0.706 V at a scan rate of 5 mV s^{-1}. In addition, there is a reduction peak at approximately -0.825 V, which may be an irreversible reduction peak, indicating that there exists an irreversible unidirectional reaction. Fig. 6b shows the CV curves of the Fe_2O_3/rGO electrode in 1 M Na_2SO_4 electrolyte at different scan rates. No redox peaks were observed, which suggests no Faradaic redox reactions of the Fe_2O_3/rGO electrode in 1 M Na_2SO_4 electrolyte. In Fig. 6c, a pair of obvious redox peaks at a scan rate of 5 mV s^{-1} in 6 M KOH is observed. The redox peak gradually weakened with increasing scan rate. This phenomenon can be attributed to electrochemical polarization. Fig. 6d shows the CV curves of the Fe_2O_3/rGO electrode in 6 M KOH with 3 M methanol at different scan rates. A pair of obvious redox peaks and an irreversible reduction peak at a scan rate of 5 mV s^{-1} were observed. Then, the irreversible reduction peak disappeared at a scan rate of 20 mV s^{-1}. The redox peaks were not obvious when the scan rate increased to 50 mV s^{-1}. This result can be explained when the contact of the ions and electrons of the electrolyte with the active material cannot be synchronized with the electron transfer of the external circuit. The CV curves of Fe_2O_3/rGO in 1 M Na_2SO_3, 1 M Na_2SO_4 and 1 M KOH at a scan rate of 10 mV s^{-1} are shown in Fig. 6e. The Fe_2O_3/rGO electrode shows a pair of obvious redox peaks in 1 M KOH electrolyte at an analogous potential region, and its enclosed CV area is larger than the other two, implying excellent electrochemical reactivity of the Fe_2O_3/rGO electrode in 1 M KOH electrolytes. The CV curves of Fe_2O_3/rGO electrode in 1 M KOH and 6 M KOH with and without 3 M methanol at a scan rate of 10 mV s^{-1} are shown in Fig. 6f. There is an obvious oxidation peak and reduction peak in the three electrolytes, indicating that the capacitance characteristics are mainly governed by Faradaic redox reactions, which possibly corresponds to the reversible conversion of Fe^{3+}/Fe^{2+} [33]. When the concentration of 1 M KOH was increased to 6 M KOH, the enclosed CV area also increased, showing that the specific capacitance of the Fe_2O_3/rGO electrode material increased in 6 M KOH electrolyte. However, the Fe_2O_3/rGO electrode exhibits a larger enclosed CV curve area and higher peak current in 6 M KOH with 3 M methanol electrolytes than without 3 M methanol electrolytes, which is mainly attributed to the electrochemical catalytic oxidation of methanol compared with previous literature [34].

It is well known that the intersection of the real axis and the starting point of the semicircle of the curve is the internal impedance of the electrochemical system. The half circle diameter of the curve is charge transfer resistance, which indicates the difficulty of charge transfer between the electrolyte interface and the active electrode material. The diagonal of the curve corresponds to the impedance of the electrolyte diffusion inside the active electrode material. Fig. 7a shows the diagrams of bare Fe_2O_3 and Fe_2O_3/rGO electrodes in 1 M KOH. In the low frequency region, both curves present a straight line, which indicates that Fe_2O_3/rGO and Fe_2O_3 have porous structures and thus comparative diffusion resistance. However, at the high frequency region, the semicircles of the two curves are completely different. The interfacial charge transfer resistance can be represented by the diameter of the semicircle: the larger the semicircle, the larger the charge-transfer resistance. Obviously, the Fe_2O_3/rGO shows a smaller semicircle than that of the Fe_2O_3 electrode, implying its lower charge-transfer resistance. Fig. 7b shows the Nyquist plots of the Fe_2O_3/rGO electrode in 1 M Na_2SO_3 and 1 M Na_2SO_4 electrolytes. The diffusion resistance and series resistance of the Fe_2O_3/rGO electrode in 1

M Na_2SO_3 is obviously smaller than that in 1 M Na_2SO_4. Fig. 7c shows the Nyquist plots of Fe_2O_3/rGO in 6 M KOH with and without 3 M methanol electrolytes. After the addition of methanol, the series resistance and diffusion resistance of the Fe_2O_3/rGO electrode both decreased. This result reveals that the Fe_2O_3/rGO electrode has better electron transfer ability in 6 M KOH with 3 M methanol electrolytes.

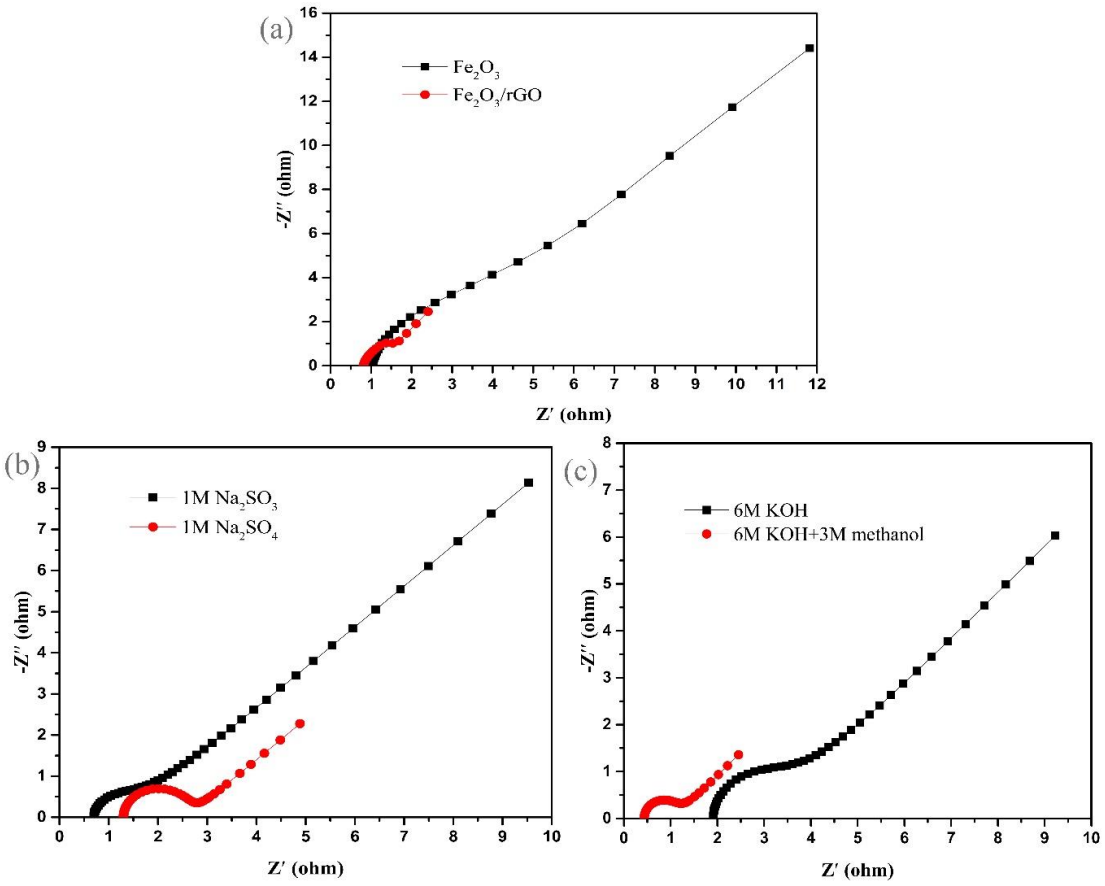

Figure 7. (a) Nyquist plots of pure Fe_2O_3 and Fe_2O_3/rGO electrodes in 1M KOH electrolytes. (b) Nyquist plots of Fe_2O_3/rGO electrode in 1M Na_2SO_3, 1M Na_2SO_4 electrolytes. (c) Nyquist plots of Fe_2O_3/rGO electrode in 6M KOH with and without 3M methanol electrolytes.

4. CONCLUSIONS

In this work, an Fe_2O_3/rGO composite was prepared by a facile hydrothermal method. In this composite, the Fe_2O_3 particles have an elliptical shape and porous structure, which greatly enhance the specific surface area compared to that of hexagonal Fe_2O_3 particles. As a supercapacitor electrode material, the specific capacitance of the Fe_2O_3/rGO composite was significantly improved compared to that of Fe_2O_3 in 1 M KOH. Such superior electrochemical performance is attributed to the porous oval structure of the Fe_2O_3 particles and excellent conductivity and high specific surface area of rGO. In addition, the Fe_2O_3/rGO electrode has better electrochemical performance in 6 M KOH with 3 M methanol because of the electrocatalytic oxidation of methanol. Therefore, the Fe_2O_3/rGO composite

has excellent electrochemical performance and can be used as the best candidate electrode material for supercapacitor energy storage devices.

ACKNOWLEDGEMENTS
This study was supported by the Priority Academic Program Development of Jiangsu Higher Education Institutions, Changzhou City of Science and Technology Support Program (CE20150042) and Qing Lan Project of Education Department of Jiangsu Province.

References

1. G. P. Wang, L. Zhang, J. J. Zhang, *Chem. Soc. Rev*., 41 (2012) 797.
2. H. P. Cong, X. C. Ren, P. Wang, S. H. Yu, *Energ. Environ. Sci.,* 6 (2013) 1185.
3. X. Peng, L. L. Peng, C. Z. Wu, Y. Xie, *Chem Soc Rev*., 43 (2014) 3303.
4. H. B. Hu, Z. b. Pei, C. H. Ye, *Energy Storage Materials.*, 1 (2015) 82.
5. S. W. Zhang, B. S. Yin, Z. B. Wang, F. Peter, *Chem. Eng. J.*, 306 (2016) 193.
6. X. Zheng, X. Q. Yan, Y. H. Sun, Y. S. Yu, G. J. Zhang, Y. W. Shen, Q. J. Liang, Q. L. Liao, Y. Zhang, *J. Colloid. Interf. Sci.,* 466 (2016) 291.
7. M. Zhang, J. Sha, X. Miao, E. Liu, C. Shi, J. Li, C. He, Q. Li, N. Zhao, *J. Alloy. Compd.,* 696 (2017) 956.
8. H. Y. Quan, B. C. Cheng, Y. H. Xiao, S. J. Lei, *Chem. Eng. J.*, 286 (2016) 165.
9. Y. Gao, D. L. Wu, T. Wang, D. Z. Jia, W. Xia, Y. Lv, Y. L. Cao, Y. Y. Tan, P. G. Liu, *Electrochim Acta.*, 191 (2016) 275.
10. H. R. Naderi, P. Norouzi, M. R. Ganjali, *Mater. Chem. Phys.*, 163 (2015) 38.
11. Z. Yu, L. Tetard, L. Zhai, J. Thomas, *Energ. Environ. Sci.*, 8 (2015) 702.
12. K. Xie, X. Qin, X. Wang, Y. Wang, H. Tao, Q. Wu, L. Yang, Z. Hu, *Adv. Mater.,* 24 (2012) 347.
13. Z. X. Song, W. Liu, W. S. Wei, C. Z. Quan, N. X. Sun, Q. Zhou, G. H. Liu, X. Q. Wen, *J. Alloy. Compd.*, 685 (2016) 355.
14. H. R. Naderi, P. Norouzi, M. R. Ganjali, *Appl. Surf. Sci.,* 366 (2016) 552.
15. F. Y. Ning, M. F. Shao, C. L. Zhang, S. M. Xu, M. Wei, X. Duan, *Nano Energy*, 7 (2014) 134.
16. Z. X. Song, W. Liu, P. Xiao, Z. F. Zhao, G. C. Liu, J. S. Qiu, *Mater. Lett.*, 145 (2015) 44.
17. Y. Z. Guo, B. B. Chang, T. Wen, C. M. Zhao, H. Yin, Y. N. Zhou, Y. G. Wang, B. C. Yang, S. R. Zhang, *Rsc. Adv*., 6 (2016) 19394.
18. K. Naoi, T. Kurita, M. Abe, T. Furuhashi, Y. Abe, K. Okazaki, J. Miyamoto, E. Iwama, S. Aoyagi, W. Naoi, *Adv. Mater.,* 28 (2016) 6751.
19. S. Shivakumara, T. R. Penki, N. Munichandraiah, *Mater. Lett.*, 131 (2014) 100.
20. Z. y. Wang, C.J. Liu, *Nano Energy*, 11(2015) 277.
21. A. Abdi, M. Trari, *Electrochim. Acta*, 111(2013) 869.
22. W. L. Yang, Z. Gao, J. Wang, B. Wang, L. Liu, *Solid. State. Sci.*, 20 (2013) 46.
23. S. Liu, S. H. Sun, X. Z. You, *Nanoscale.*, 6 (2014) 2037.
24. S. William, J. R. Hummers, R. E. Offeman, *J. Am. Chem. Soc.*, 80 (1958) 1339.
25. G. K. Pradhan, D. K. Padhi, K. M. Parida, *ACS Appl. Mater. Interfaces.*, 5 (2013) 9101.
26. H. W. Wang, Z. J. Xu, H. Yi, H. G. Wei, Z. H. Guo, X. F. Wang, *Nano Energy.*, 7 (2014) 86.
27. M. S. Dresselhaus, A. Jorio, M. Hofmann, G. Dresselhaus, R. Saito, *Nano Lett.*, 10 (2010) 751.
28. S. Nag, A. Roychowdhury, D. Das, S. Mukherjee, *Mater. Res. Bull.*, 74 (2016) 109.
29. Q. Qu, S.Yang, X.Feng, *Adv.Mater.*, 23 (2011) 5574.
30. B. T. Hanga, T. Watanabe, M. Eashira, S. Okada, J. I.Yamaki, S. Hata, S. H. Yoon, I. Mochida, *J. PowerSources.*, 150 (2005) 261.
31. H. Wang, Z. Xu, H. Yi, H. Wei, Z. Guo, X. Wang, *Nano Energy.*, 7 (2014) 86.

32. H. G. Ranjbar, M. R. Ganjali, P. Norouzi, H. R. Naderi, *Ceram Int.,* 4 (2016) 140.
33. T. W. C. L. Long, J. Yan, L. L. Jiang, Z. J. Fan, *Acs Nano.,* 7 (2013) 11325.
34. M. Yu, J. P. Chen, J. H. Liu, S. M. Li, Y. X. Ma, J. D. Zhang, J. W. An, *Electrochim Acta.,* 151 (2015) 99.